



Simultaneous fluorescence and Compton scattering computed tomography based on linear polarization X-ray

Zhi-Jun Chi¹ · Hong-Ze Zhang² · Jin Lin² · Xuan-Qi Zhang² · Hao Ding² · Qi-Li Tian² · Zhi Zhang² · Ying-Chao Du² · Wen-Hui Huang² · Chuan-Xiang Tang²

Received: 21 December 2023 / Revised: 29 February 2024 / Accepted: 14 March 2024 / Published online: 21 September 2024

© The Author(s), under exclusive licence to China Science Publishing & Media Ltd. (Science Press), Shanghai Institute of Applied Physics, the Chinese Academy of Sciences, Chinese Nuclear Society 2024

Abstract

Purpose To propose a method for simultaneous fluorescence and Compton scattering computed tomography by using linearly polarized X-rays.

Methods Monte Carlo simulations were adopted to demonstrate the feasibility of the proposed method. In the simulations, the phantom is a polytetrafluoroethylene cylinder inside which are cylindrical columns containing aluminum, water, and gold (Au)-loaded water solutions with Au concentrations ranging between 0.5 and 4.0 wt%, and a parallel-hole collimator imaging geometry was adopted. The light source was modeled based on a Thomson scattering X-ray source. The phantom images for both imaging modalities were reconstructed using a maximumlikelihood expectation maximization algorithm.

Results Both the X-ray fluorescence computed tomography (XFCT) and Compton scattering computed tomography (CSCT) images of the phantom were accurately reconstructed. A similar attenuation contrast problem for the different cylindrical columns in the phantom can be resolved in the XFCT and CSCT images. The interplay between XFCT and CSCT was analyzed, and the contrast-to-noise ratio (CNR) of the reconstruction was improved by correcting for the mutual influence between the two imaging modalities. Compared with K-edge subtraction imaging, XFCT exhibits a CNR advantage for the phantom.

Conclusion Simultaneous XFCT and CSCT can be realized by using linearly polarized X-rays. The synergy between the two imaging modalities would have an important application in cancer radiation therapy

Keywords X-ray fluorescence computed tomography · Compton scattering computed tomography · Linear polarization · Thomson scattering X-ray source · Monte Carlo simulation

1 Introduction

Since Godfrey N. Hounsfield constructed the first clinical X-ray computed tomography (XCT) scanner in the early 1970s [1], XCT imaging has become an indispensable tool in various fields including medical diagnostics, proton

therapy [2], industrial non-destructive testing [3], and materials science. Over the past 50 years, the XCT image quality has improved tremendously. However, materials with similar X-ray attenuation cannot exhibit distinguishable contrast in XCT. Because the reconstructed linear attenuation coefficient distribution of an imaging object in XCT is determined by many factors, such as the X-ray energy, material mass density, and elemental composition [4–12], it is easy for different materials to possess a similar X-ray attenuation, particularly when a broad energy spectrum produced by conventional X-ray tubes is used. Therefore, it is necessary to develop multiple imaging modalities to provide a comprehensive description of the imaging object.

X-ray fluorescence computed tomography (XFCT) and Compton scattering computed tomography (CSCT) can provide more valuable information regarding the imaging object than the linear attenuation coefficient in

This work was supported by the National Natural Science Foundation of China (Nos. 12375157, 12027902, and 11905011).

✉ Zhi-Jun Chi
chizj18@bnu.edu.cn

¹ Key Laboratory of Beam Technology of the Ministry of Education, School of Physics and Astronomy, Beijing Normal University, Beijing 100875, China

² Key Laboratory of Particle and Radiation Imaging of the Ministry of Education, Department of Engineering Physics, Tsinghua University, Beijing 100084, China

XCT, which helps resolve the above-mentioned material discrimination problem in XCT. In XFCT, the contrast agent distribution and its quantitative concentration can be reconstructed simultaneously, providing a novel method for molecular imaging [13–20], and is expected to become a promising method for early cancer detection with the application of nanoparticles such as Au and Gd. In CSCT, the electron density distribution of the imaging object can be reconstructed [21], which plays a crucial role in accurate radiation dose calculation [22, 23] and range estimation [24–27] in charged-particle therapy treatment planning. The distribution of both contrast agents in XFCT and electron density in CSCT can help extend the ability of material discrimination, and the synergy between them would have an important application in cancer radiation therapy, as high-resolution and high-sensitivity cancer diagnosis via XFCT and high-accuracy dose calculation and range estimation via CSCT can be realized simultaneously. However, XFCT and CSCT cannot be realized simultaneously because distinguishing one signal from another is intractable. For example, special efforts must be made to reduce the influence of a strong Compton scattering background in XFCT [14, 17, 19, 20, 28], as it has a significant impact on image quality.

With the rapid development of Thomson scattering (also called inverse Compton scattering in the gamma-ray energy region when the electron recoil cannot be neglected), polarization-tunable X-rays can be easily generated [29–31], providing a novel polarization-based method for Compton scattering background suppression in XFCT [32]. Using linearly polarized X-rays, X-ray fluorescence and Compton scattering signals can be distinguished; therefore, it is possible to realize XFCT and CSCT simultaneously. In this study, the feasibility of simultaneous XFCT and CSCT based on linearly polarized X-rays was investigated using Monte Carlo (MC) simulations. The interplay between XFCT and CSCT was analyzed, and effective methods to correct this mutual influence were developed. Finally, a comparison between the two imaging modalities and *K*-edge subtraction imaging is presented and discussed.

2 Methods

2.1 Principle of simultaneous XFCT and CSCT

To realize simultaneous XFCT and CSCT, the X-ray fluorescence and Compton scattering signals must be distinguishable, which can be achieved using linearly polarized X-rays. For linearly polarized X-rays, the differential Compton scattering cross section is described by the Klein–Nishina formula:

$$\frac{d\sigma_{\text{KN,LP}}}{d\Omega}(E_0) = \frac{1}{2} r_e^2 \epsilon^2 (\epsilon + \epsilon^{-1} - 2 \sin^2 \theta \cos^2 \phi), \quad (1)$$

where r_e is the classical electron radius, θ and ϕ are the polar and azimuthal angles, respectively, and

$$\epsilon = \frac{E_f}{E_0} = \frac{1}{1 + \frac{E_0}{m_e c^2} (1 - \cos \theta)}, \quad (2)$$

where E_f and E_0 are the Compton-scattered and incident photon energies, respectively, and $m_e c^2$ is the rest energy of an electron. Obviously, the differential Compton scattering cross section is ϕ -dependent; therefore, it can be increased or decreased by adjusting the polarization direction of the incident X-rays.

For XFCT and CSCT, the signal detector is typically placed perpendicular to the incident X-ray beam, for example, $\theta = 90^\circ$. In this direction, the differential Compton scattering cross section reaches its minimum and maximum values at $\phi = 0^\circ/180^\circ$ and $\phi = 90^\circ/270^\circ$, respectively, as shown in Fig. 1. If the signal detector is arranged in the *x*-axis direction, a single Compton scattering background can be completely suppressed using incident X-rays with horizontal polarization (*x*-axis direction), and the X-ray fluorescence projection P_{XFCT} used for XFCT reconstruction can be obtained. Furthermore, when the incident X-ray polarization changes to the vertical direction (*y*-axis), the Compton scattering projection $P_{\text{CS,VP}}$ that is intermingled with the X-ray fluorescence background is acquired. Usually, the energy difference between an X-ray fluorescence photon and a Compton-scattered photon is not distinct; therefore, they cannot be distinguished via photon energy. However, if the two projections are taken at the same photon flux and scan time, the Compton scattering projection P_{CSCT} used for CSCT reconstruction can be obtained by subtracting the Compton scattering projection $P_{\text{CS,HP}}$ obtained in the horizontal polarization case from the Compton scattering projection $P_{\text{CS,VP}}$, i.e., $P_{\text{CSCT}} = P_{\text{CS,VP}} - P_{\text{CS,HP}}$. ($P_{\text{CS,VP}}$ and

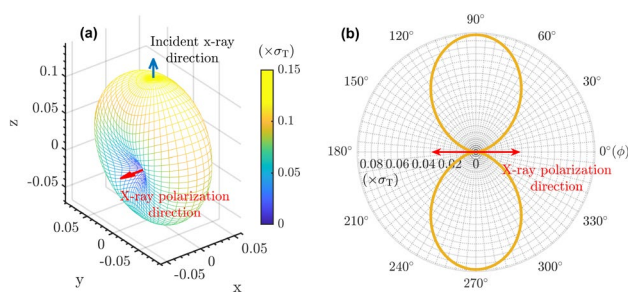


Fig. 1 (Color online) Differential Compton scattering cross-section distribution at (a) the full space and (b) $\theta = 90^\circ$ plane. The incident X-ray energy is 83 keV, and σ_T is the total Thomson scattering cross section

$P_{CS,HP}$ are acquired at the same energy region.) Thus, XFCT and CSCT can be realized simultaneously.

2.2 Monte Carlo simulations

To demonstrate the feasibility of the simultaneous XFCT and CSCT, MC simulations were performed using the Geant4 toolkit [33]. The image layout is shown in Fig. 2. The X-ray source was modeled based on a Thomson scattering light source that can provide quasi-monochromatic, continuously energy-tunable, and polarization-controllable X-rays. To satisfy the field-of-view (FOV) requirements of a small-animal-sized imaging object (~ 5 cm) and quasi-monochromatic spectral conditions, a large source-to-sample distance is required for Thomson scattering light sources [32, 34]. To simplify the unnecessary X-ray transport before the phantom, a quasi-parallel X-ray beam (2D) was adopted in the MC simulations, which was incident on the phantom along the +z axis. The X-ray spectrum has a Gaussian distribution with a peak energy of $E_0 = 83$ keV and an RMS bandwidth of 1.5%, which can be easily achieved using existing technologies [35, 36]. The incident X-rays are linearly polarized, and their polarization is tunable between the horizontal (x-axis) and vertical directions (y-axis).

The phantom was a polytetrafluoroethylene (Teflon) cylinder with a diameter of 5.0 cm. Inside the Teflon cylinder were six cylindrical columns 1.0 cm in diameter, containing aluminum (Al), water (H₂O), and gold (Au)-loaded water solution contrast agents. In the contrast agents, the Au weight fractions were 0.5, 1.0, 2.0, and 4.0 wt%, respectively. For Au, its K – edge E_K is located at 80.72 keV [37] and its K_α lines generated by the Livermore library in Geant4 are 69.038 and 67.184 keV for $K_{\alpha 1}$ and $K_{\alpha 2}$, respectively.

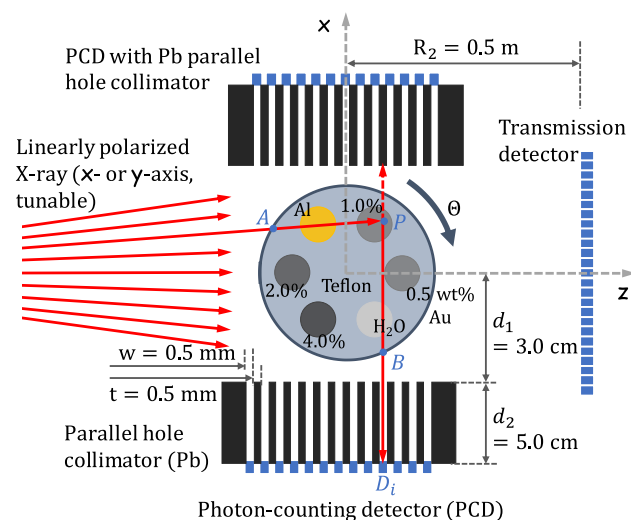


Fig. 2 (Color online) Imaging layout for simultaneous XFCT and CSCT based on linear polarization X-rays (not to scale)

For fluorescent and Compton-scattered X-ray photon detection, a photon-counting detector (PCD) was placed perpendicular to the x-axis in the x – z plane, and the distance between the PCD and the center of the phantom was 8.0 cm. The PCD was modeled with a pixel size of 0.5 mm and a sensitive energy range of 20–100 keV; currently, these performances can be easily achieved [38]. For simplicity, the energy resolution and detection efficiency of the PCD were assumed ideal. A parallel-hole collimator made of lead (Pb) was placed at the front of the PCD. The length (x-axis direction) and opening size (z-axis direction) of the collimator are 5.0 cm and 0.5 mm, respectively. To improve the fluorescent and Compton-scattered X-ray photon detection efficiency and to improve the XFCT and CSCT reconstruction spatial resolution, a second PCD combined with a parallel-hole collimator was placed on the opposite side of the phantom, and the parallel-hole collimator was offset from the first one by half of the parallel-hole pitch, as shown in Fig. 2. To correct the phantom attenuation in XFCT and CSCT, an ideal transmission detector with a pixel size of 0.2 mm was placed 0.5 m downstream of the phantom to acquire the phantom attenuation data.

In the MC simulations, 360-deg projections were acquired at a rotational step of 1° for the CT scan. To balance statistical error and simulation time, 5×10^9 photons were used for each projection.

2.3 Image reconstruction

Based on the imaging geometry in Fig. 2, the fluorescent and Compton-scattered X-ray photon detection can be divided into three steps.

- Stimulation of fluorescent and Compton-scattered X-ray photons in the phantom

As the incident X-ray travels from point A to point P to stimulate the fluorescent and Compton-scattered X-ray photons, the beam intensity is attenuated by the phantom,

$$I(P) = I_0 \exp \left[- \int_A^P \mu(E_0, \vec{r}) ds \right], \tag{3}$$

where $I(P)$ and I_0 are the X-ray beam intensities at points A and P, respectively, μ is the linear attenuation coefficient of the phantom, E_0 is the incident X-ray energy, and \vec{r} is the spatial position vector.

- Emission of fluorescent and Compton-scattered X-ray photons

If Au is located at point P, the K_α fluorescence of Au is emitted isotropically as E_0 is higher than E_K . The differential intensity of fluorescent X-ray photons can be written as

$$\frac{dI_{\text{XRF}}}{d\Omega}(P) = \frac{1}{4\pi} I(P) \mu_{\text{Au,PE}}^m(E_0) \rho_{\text{Au}}(P) \omega_{K_\alpha}, \tag{4a}$$

where $\mu_{\text{Au,PE}}^m(E_0)$ is the photoelectric mass absorption coefficient of Au at X-ray energy E_0 , $\rho_{\text{Au}}(P)$ is the local Au concentration (in mass percent) to be reconstructed in XFCT, and ω_{K_α} is the fluorescence yield of Au. Meanwhile, the Compton-scattered X-ray photons are also emitted and their spatial distribution is governed by the differential cross-section Eq. (1). The differential intensity of Compton-scattered X-ray photons can be written as

$$\frac{dI_{\text{CS}}}{d\Omega}(P) = I(P) \rho_e(P) \frac{d\sigma_{\text{KN,LP}}}{d\Omega}(E_0), \tag{4b}$$

where $\rho_e(P)$ is the local electron density to be reconstructed in CSCT.

- Detection of the fluorescent and Compton-scattered X-ray photons by the PCD

After passing through the parallel-hole collimator, the fluorescent and Compton-scattered X-ray photons are finally detected by the PCD. Along this path, the beam intensity is attenuated by the phantom from point P to boundary B . Therefore, the beam intensity of fluorescent and Compton-scattered X-ray photons coming from P and detected at detector pixel bin D_i can be described as

$$I_{\text{det},u}(P, D_i) = \frac{dI_u}{d\Omega}(P) \Delta\Omega_{c,i} \times \exp \left[- \int_P^B \mu(E_u, \vec{r}) ds \right], \tag{5}$$

where the subscript 'u' indicates XRF or CS for fluorescent or Compton-scattered X-ray photons, respectively, similarly, hereinafter, E_{XRF} and E_{CS} are the photon energies of the fluorescent and Compton-scattered X-ray photons, respectively, and $\Delta\Omega_{c,i}$ is the collecting angle of the parallel-hole collimator corresponding to detector pixel bin D_i .

According to the fluorescent and Compton-scattered X-ray photon detection process, the total fluorescent or Compton-scattered beam intensity detected at D_i can be described as a volume integral of $I_{\text{det},u}(P, D_i)$:

$$I_{u,i} = \int \int \int V_{P \rightarrow D_i} I_{\text{det},u}(P, D_i) dV_P, \tag{6}$$

where the integration domain $V_{P \rightarrow D_i}$ is the phantom region subtended by D_i toward the parallel-hole collimator. For both XFCT and CSCT, the detected signal intensity \mathbf{I} of size $M \times 1$ and the unknown parameters \mathbf{p} (ρ_{Au} or ρ_e) of size $N \times 1$ to be reconstructed can be uniformly expressed as a system of linear equations:

$$\mathbf{I} = \mathbb{A}\mathbf{p}, \tag{7}$$

where $\mathbb{A} = [a_{ij}]_{M \times N}$ is a system matrix of size $M \times N$. Similar to other emission tomography techniques (e.g., SPECT and PET), the detected X-ray photon number is relatively low in both XFCT and CSCT, and statistical noise is the major limiting factor for accurate reconstruction. To reduce statistical noise artifacts, the \mathbf{p} distribution was reconstructed using the commonly used maximum-likelihood expectation maximization (MLEM) algorithm [39] for emission tomography,

$$\rho_j^{(k+1)} = \frac{\rho_j^{(k)}}{\sum_{i=1}^M a_{ij}} \sum_{i=1}^M \frac{a_{ij} I_i}{\sum_{j'=1}^N a_{ij'} \rho_{j'}^{(k)}} \quad (j = 1, 2, \dots, N). \tag{8}$$

To obtain an accurate system matrix \mathbb{A} , the attenuation terms $\mu(E_0, \vec{r})$ in Eq. (3) and $\mu(E_u, \vec{r})$ in Eq. (5) must be determined, which can be realized using a transmission CT scan of the phantom at the corresponding X-ray energy. For the attenuation CT, statistical noise is not the limiting factor for accurate reconstruction because the signal-to-noise ratio (SNR) in the projections is relatively high. Therefore, the well-known ART-TV iterative algorithm, proven to be effective in our laboratory, was adopted for CT reconstruction at different X-ray energies, and 180 projections taken at a rotational step of 1° were used.

3 Results and discussion

To realize simultaneous XFCT and CSCT, it is essential to distinguish between fluorescence and Compton scattering X-ray signals using linear polarization X-rays. To examine the feasibility of the proposed method, the PCD detected X-ray spectra at both horizontal and vertical X-ray polarizations were compared using the MC simulation results, as shown in Fig. 3a. The spectra were acquired by summing all the pixels of the PCD with an ideal energy resolution after a full CT scan. As shown in Fig. 3a, single Compton scattering can be significantly improved or suppressed in the vertical or horizontal X-ray polarizations, respectively, as predicted by the Compton scattering theory described in Sect. 2.1. Because single Compton scattering is suppressed in the case of horizontal polarization, the X-ray fluorescence projection used for XFCT reconstruction can be obtained directly by selecting a suitable detection-energy region for the PCD. In the MC simulations, the PCD energy region used for X-ray fluorescence detection was set to 67–69.5 keV. The Compton scattering signal was obtained by subtracting the horizontal polarization spectrum from the vertical polarization spectrum, as shown in Fig. 3b. Considering the influence of multiple scattering and Doppler broadening

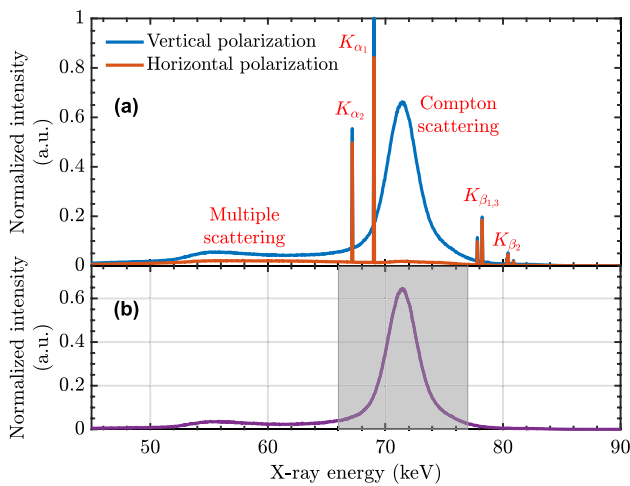


Fig. 3 (Color online) *a* X-ray spectra detected by the PCD at the horizontal and vertical polarizations and *b* Compton scattering spectrum obtained by subtracting the horizontal polarization spectrum from the vertical polarization spectrum. The gray energy region in *b* depicts the effective Compton scattering energy region used to generate the CSCT projection

caused by electron motion, an effective Compton scattering energy region ranging from 66 to 77 keV was selected, as shown in the gray region in Fig. 3b, and the Compton

scattering signal in this effective-energy region was used to generate the projection for CSCT reconstruction.

After obtaining the XFCT and CSCT projections by changing the X-ray polarization, the XFCT and CSCT of the phantom were reconstructed simultaneously. The results are shown in Fig. 4. Also shown in Fig. 4 are the attenuation CT of the phantom reconstructed at X-ray peak energies of $E_0 = 83$ keV, $E_{CS} = 71.40$ keV, and $E_{XRF} = 68.13$ keV with the same rms bandwidth of 1.5%. The attenuation CT data of the phantom were used to accurately calculate the terms $\mu(E_0, \mathbf{r})$, $\mu(E_{CS}, \mathbf{r})$, and $\mu(E_{XRF}, \mathbf{r})$ in the system matrix \mathbb{A} . In the attenuation CT, Al and the contrast agent with an Au concentration of 4.0% exhibited a similar attenuation contrast at an X-ray energy of 83 keV; meanwhile, H₂O and the contrast agents with 0.5% and 1.0% Au concentrations also exhibited a similar attenuation contrast at X-ray energies of 71.40 and 68.13 keV. Therefore, these materials could not be distinguished in the corresponding attenuation CT. However, they can be easily discriminated using XFCT, as shown in Fig. 4a. Furthermore, Al and the contrast agent with 4.0% Au concentration can also be easily discriminated in CSCT owing to their large electron density difference, as shown in Fig. 4(c).

To quantitatively analyze the reconstruction results, seven regions of interest (ROIs), depicted by the pink dotted

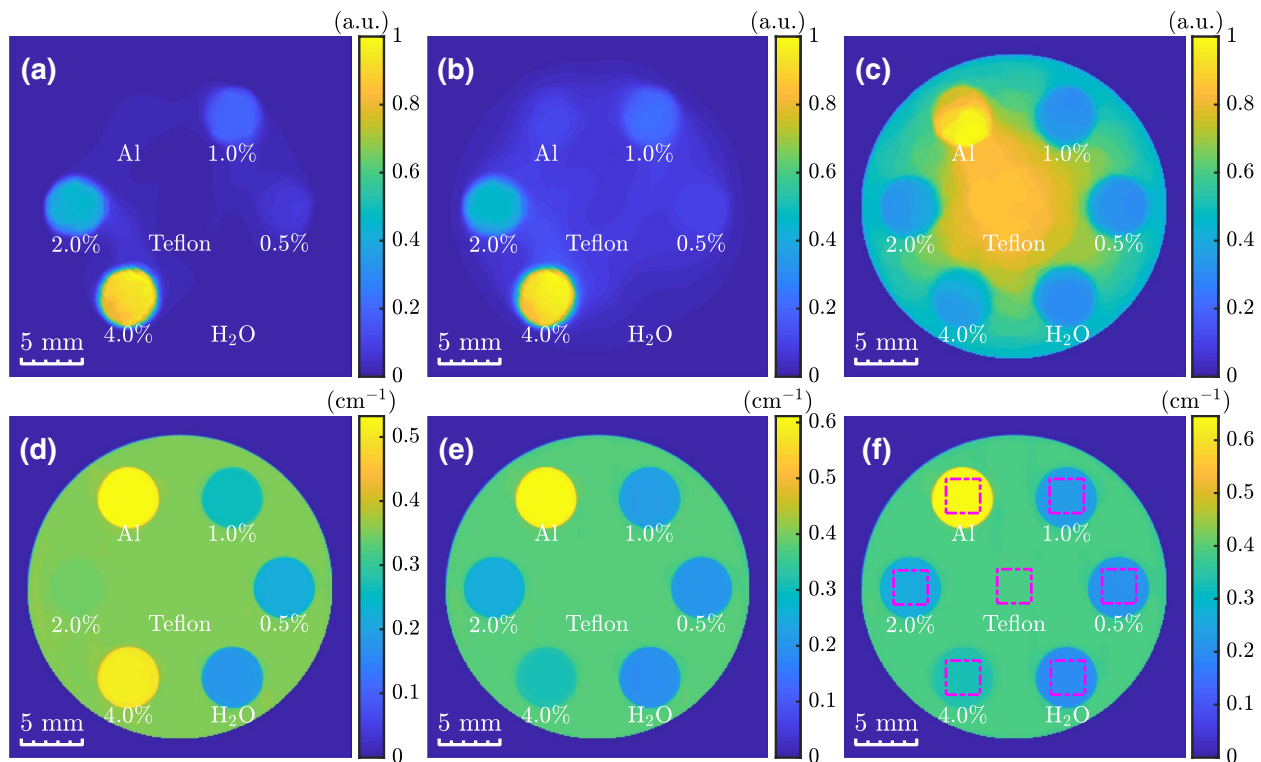


Fig. 4 (Color online) XFCT of the phantom reconstructed *a* with and *b* without multiple Compton scattering correction, *c* CSCT of the phantom, and attenuation CT of the phantom reconstructed at X-ray

peak energies of *d* 83, *e* 71.40, and *f* 68.13 keV. The pink dotted squares in *f* are ROIs chosen for quantitative analysis of the results

squares in Fig. 4f, were chosen. For XFCT, the reconstructed S value of the contrast agents, averaged over the ROI in Fig. 4a, was compared with the actual Au concentration ρ_{Au} , and the results are shown in Fig. 5. Also shown in Fig. 5 is the linear fitting result. It can be clearly seen that S and ρ_{Au} have a good linear relationship, with $r^2 = 0.9999$.

3.1 Influence of multiple Compton scattering on XFCT

Although single Compton scattering can be greatly suppressed using horizontally polarized X-rays, multiple Compton scattering can still have an impact on XFCT. As shown in Fig. 4b, the XFCT reconstruction quality, compared with the multiple Compton scattering correction result in Fig. 4a,

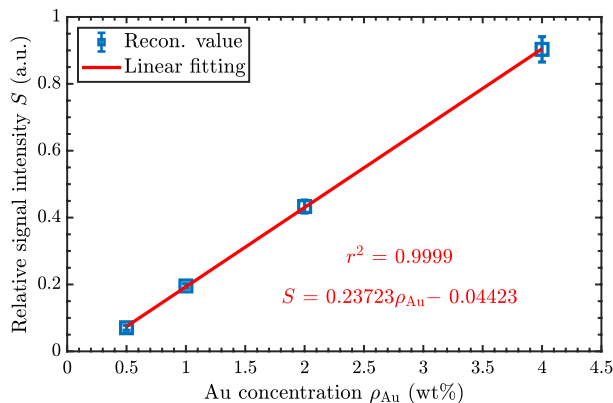


Fig. 5 Relation between the reconstructed result S , averaged over the ROI, and the actual Au concentration. The error bar was calculated using the corresponding standard deviation

deteriorates owing to the influence of multiple Compton scattering. An effective method was developed to correct for this influence. Considering that multiple Compton scattering is almost uniformly distributed in the X-ray spectrum, as shown in Fig. 3a, the multiple Compton scattering MS_{XRF} in the X-ray fluorescence detection energy region can be calculated via linear interpolation:

$$MS_{\text{XRF}} = \frac{1}{2}(MS_- + MS_+), \quad (9)$$

where MS_- and MS_+ are the multiple Compton scattering intensities in the low (64.5–67 keV) and high (69.5–72 keV) regions, respectively. The multiple Compton scattering correction was realized by subtracting MS_{XRF} from the X-ray fluorescence signal detected by the PCD in the horizontal polarization case.

To quantitatively evaluate the contrast improvement caused by multiple Compton scattering correction, the contrast-to-noise ratio (CNR) is calculated as

$$\text{CNR} = \frac{S_{\text{Au}} - S_{\text{BG}}}{\sigma_{\text{BG}}}, \quad (10)$$

where S_{Au} and S_{BG} are the mean values of S in the Au and Teflon ROI, respectively, and σ_{BG} is the standard deviation in the Teflon ROI. The calculated CNR results for the different materials are shown in Fig. 6. Also depicted in Fig. 6 is the limit of detection ($\text{CNR} = \pm 5$) based on the Rose criterion [40]. It can be seen that the CNR values of the four contrast agents, especially the contrast agent with 0.5% Au concentration, are greatly improved by the multiple Compton scattering correction. Without multiple Compton scattering correction, Al becomes detectable in XFCT (CNR

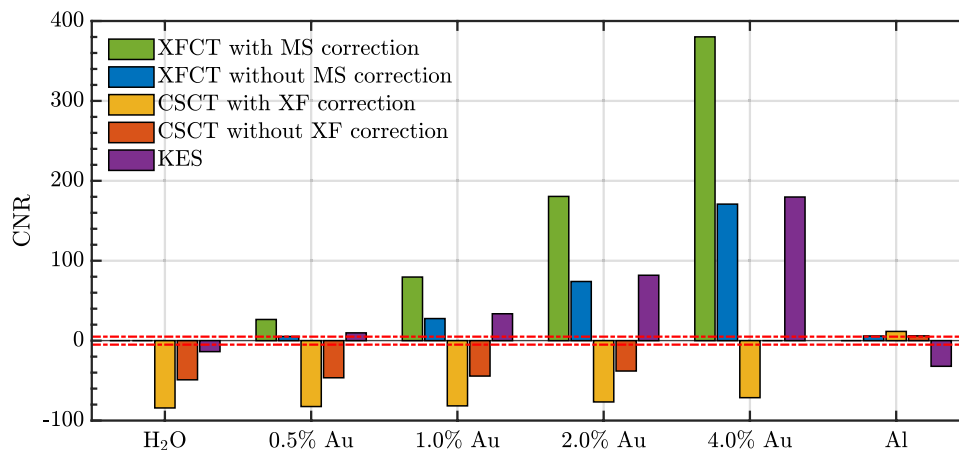


Fig. 6 (Color online) CNR comparison between XFCT, CSCT, and KES. MS: multiple scattering; XF: X-ray fluorescence. The red dot-dashed lines describe the limit of detection ($\text{CNR} = \pm 5$) according to the Rose criterion. The data of H_2O in XFCT, contrast agent with

4.0% Au concentration in CSCT without XF correction, and Al in XFCT with MS correction are not depicted because they cannot be identified by their geometric shape in the corresponding reconstruction images. (Color figure online)

= 5.84), which does not reflect the real situation because this column has no Au. After multiple Compton scattering correction, Al could not be discriminated from the background, as shown in Fig. 4a. Therefore, it is necessary to correct for the multiple Compton scattering background to improve the CNR in XFCT.

3.2 Influence of X-ray fluorescence on CSCT

Compared with the Compton scattering signal covering a relatively wide energy region, the integrated X-ray fluorescence background was very weak in the vertical polarization case, as shown in Fig. 3a. However, this weak X-ray fluorescence background can still affect the CSCT reconstruction quality. For comparison, the CSCT of the phantom was reconstructed without subtracting the X-ray fluorescence background acquired for horizontal polarization. The reconstruction results are presented in Fig. 7. Clearly, the contrast agent with 4.0% Au concentration cannot be discriminated from its surrounding background owing to the influence of X-ray fluorescence. To quantitatively analyze the influence of X-ray fluorescence background on CSCT, the CNR was calculated, and the results are shown in Fig. 6. It can be seen that the CNR values of Al, H₂O, and the three contrast agents with lower Au concentrations are improved approximately 1.9-fold on average after the X-ray fluorescence correction. In addition, the CSCT reconstruction results are also influenced by serious artifacts, especially in the central Teflon area, as shown in Figs. 4c and 7. Unlike XFCT, in which only contrast agents can emit effective signals, all the materials in the phantom can produce Compton scattering

signals in CSCT. For accurate CSCT reconstruction, projections of different materials with a higher SNR are required, and the strong statistical noise of the background material (i.e., Teflon) (while the fluorescence signal is sufficiently high for accurate XFCT reconstruction at the same photon flux) may cause these artifacts. Therefore, effective methods for CSCT reconstruction with a lower SNR should be developed to correct the artifacts in future studies. Owing to the influence of reconstruction artifacts, Al without X-ray fluorescence background correction can hardly be discriminated from the background (CNR~ 5, see Fig. 6), whereas it can be easily identified (CNR = 11.56) after the X-ray fluorescence correction.

3.3 Comparison with *K*-edge subtraction imaging

K-edge subtraction (KES) is an effective imaging modality for medical diagnosis that uses the *K*-absorption edge discontinuity of the contrast agent [41]. For this application, the Thomson scattering light source has proven to be an excellent tool owing to its quasi-monochromaticity, energy tunability, and high brightness [42–46]. Previous studies using broad-spectrum X-ray tubes demonstrated that the CNR of KES is lower than that of XFCT when the contrast agent concentration is lower than 0.4% [47, 48]. However, this conclusion can be influenced by many factors, including the X-ray spectrum, imaging geometry, phantom type, and reconstruction method. To confirm our prediction, the KES results were analyzed using our imaging layout. Because the attenuation CT of the phantom was reconstructed at X-ray energies above and below the *K*-edge of Au in our simulation, the KES image of the phantom could be obtained at the same radiation dose level,

$$\Delta\mu(\vec{r}) = \mu(E_K^+, \vec{r}) - \mu(E_K^-, \vec{r}), \quad (11)$$

where $E_K^+ = E_0$ and $E_K^- = E_{\text{XRF}}$ are adopted. The KES image of the phantom is shown in Fig. 8, and the CNR is shown in Fig. 6. Compared with CSCT, the four contrast agents and H₂O exhibited quite different contrasts in KES, whereas these materials exhibited a similar contrast in CSCT because of their similar electron density values. Compared with XFCT, the CNR values of the four contrast agents in KES are reduced by 2.7, 2.4, 2.2, and 2.1 times for 0.5%, 1.0%, 2.0%, and 4.0% Au concentrations, respectively. Based on the available CNR data, further extrapolation and interpretation show that the limits of detection for Au concentration (CNR value = 5) are 0.27% and 0.4% for XFCT and KES, respectively, as shown in Fig. 9. However, when the Au concentration was further reduced to 0.19%, the contrast agent could be distinguished from the background in the KES image (CNR value ≤ -5 ; see the H₂O column in Fig. 8). The anomalous CNR superiority of KES over XFCT at ultralow

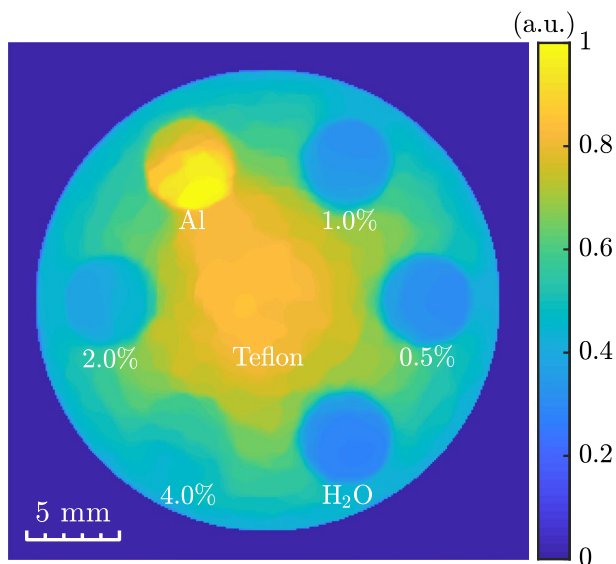


Fig. 7 (Color online) CSCT of the phantom without X-ray fluorescence background correction

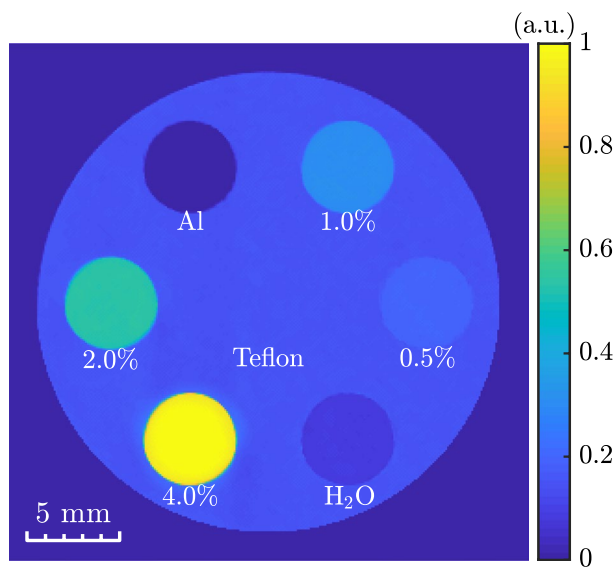


Fig. 8 (Color online) KES of the phantom

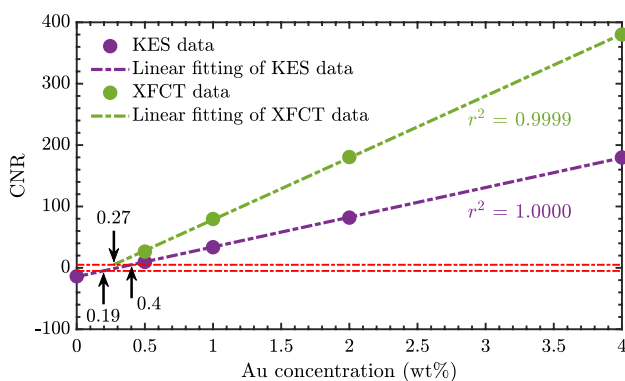


Fig. 9 (Color online) Relation between CNR and Au concentration for XFCT and KES. The red dot-dashed lines describe the limit of detection ($CNR = \pm 5$) according to the Rose criterion. (Color figure online)

Au concentrations is attributed to the large energy difference between E_K^- and E_K^+ , which causes an attenuation difference between H_2O and Teflon at the two X-ray energies.

4 Conclusion

Quasi-monochromatic, continuously energy-tunable, and straightforwardly polarization-controllable X-rays produced by Thomson scattering light sources provide excellent probes for polarization-based X-ray imaging. A method for simultaneous fluorescence and Compton scattering computed tomography using linear polarization X-rays was proposed, and its feasibility was demonstrated via Monte Carlo

simulations. Owing to the influence of multiple Compton scattering, the contrast-to-noise ratio (CNR) of X-ray fluorescence computed tomography (XFCT) deteriorated, and an effective method for multiple Compton scattering correction based on simple linear interpolation was developed. Although the integrated intensity of X-ray fluorescence is very weak compared to Compton scattering, its influence on Compton scattering computed tomography (CSCT), especially for contrast agents with high Au concentrations, cannot be neglected. Compared with *K*-edge subtraction (KES) imaging, CSCT shows a poor material identification ability for contrast agents with Au concentrations ranging from 0.5 to 4.0 wt%, while XFCT exhibits a CNR advantage for the same contrast agents.

Author contributions All authors contributed to the study conception and design. Material preparation, data collection, and analysis were performed by Zhi-Jun Chi, Hong-Ze Zhang, Jin Lin, Xuan-Qi Zhang, Hao Ding, and Qi-Li Tian. The first draft of the manuscript was written by Zhi-Jun Chi, and all authors commented on previous versions of the manuscript. All authors read and approved the final manuscript.

Data availability The data that support the findings of this study are openly available in Science Data Bank at <https://cstr.cn/31253.11.sciencedb.j00186.00183> and <https://www.doi.org/10.57760/sciencedb.j00186.00183>.

Declarations

Conflict of interest The authors declare that they have no conflict of interest.

References

- G.N. Hounsfield, Computerized transverse axial scanning (tomography): Part 1. *Descr. Syst. Br. J. Radiol.* **46**, 1016 (1973). <https://doi.org/10.1259/0007-1285-46-552-1016>
- Y.Q. Yang, W.C. Fang, X.X. Huang et al., A new imaging mode based on X-ray CT as prior image and sparsely sampled projections for rapid clinical proton CT. *Nucl. Sci. Tech.* **34**, 126 (2023). <https://doi.org/10.1007/s41365-023-01280-6>
- H.Y. Lan, T. Song, Z.H. Luo et al., Isotope-sensitive imaging of special nuclear materials using computer tomography based on scattering nuclear resonance fluorescence. *Phys. Rev. Appl.* **16**, 054048 (2021). <https://doi.org/10.1103/PhysRevApplied.16.054048>
- R.E. Alvarez, A. Macovski, Energy-selective reconstructions in x-ray computerised tomography. *Phys. Med. Biol.* **21**, 733 (1976). <https://doi.org/10.1088/0031-9155/21/5/002>
- D. Hawkes, D. Jackson, An accurate parametrisation of the X-ray attenuation coefficient. *Phys. Med. Biol.* **25**, 1167 (1980). <https://doi.org/10.1088/0031-9155/25/6/014>
- D.F. Jackson, D.J. Hawkes, X-ray attenuation coefficients of elements and mixtures. *Phys. Rep.* **70**, 169 (1981). [https://doi.org/10.1016/0370-1573\(81\)90014-4](https://doi.org/10.1016/0370-1573(81)90014-4)
- R.G. Ouellet, L.J. Schreiner, A parametrization of the mass attenuation coefficients for elements with $Z=1$ to $Z=92$ in the photon energy range from approximately 1 to 150 keV. *Phys. Med. Biol.* **36**, 987 (1991). <https://doi.org/10.1088/0031-9155/36/7/007>

8. P. Sukovle, N. Clinthorne, Basis material decomposition using triple-energy X-ray computed tomography. *IMTC/99* **3**, 1615–1618 (1999). <https://doi.org/10.1109/IMTC.1999.776097>
9. S.M. Midgley, A parameterization scheme for the X-ray linear attenuation coefficient and energy absorption coefficient. *Phys. Med. Biol.* **49**, 307 (2004). <https://doi.org/10.1088/0031-9155/49/2/009>
10. E. Roessl, R. Proksa, K-edge imaging in X-ray computed tomography using multi-bin photon counting detectors. *Phys. Med. Biol.* **52**, 4679 (2007). <https://doi.org/10.1088/0031-9155/52/15/020>
11. J. Schlomka, E. Roessl, R. Dorscheid et al., Experimental feasibility of multi-energy photon-counting K-edge imaging in pre-clinical computed tomography. *Phys. Med. Biol.* **53**, 4031 (2008). <https://doi.org/10.1088/0031-9155/53/15/002>
12. Y.X. Xing, L. Zhang, X.H. Duan et al., A reconstruction method for dual high-energy CT with MeV X-rays. *IEEE T. Nucl. Sci.* **58**, 537 (2011). <https://doi.org/10.1109/TNS.2011.2112779>
13. T. Sasaya, N. Sunaguchi, K. Hyodo et al., Multi-pinhole fluorescent X-ray computed tomography for molecular imaging. *Sci. Rep.* **7**, 5742 (2017). <https://doi.org/10.1038/s41598-017-05179-2>
14. B.L. Jones, N. Manohar, F. Reynoso et al., Experimental demonstration of benchtop X-ray fluorescence computed tomography (XFCT) of gold nanoparticle-loaded objects using lead-and tin-filtered polychromatic cone-beams. *Phys. Med. Biol.* **57**, N457 (2012). <https://doi.org/10.1088/0031-9155/57/23/N457>
15. Q. Yang, B. Deng, G.H. Du et al., X-ray fluorescence computed tomography with absorption correction for biomedical samples. *X-Ray Spectrom.* **43**, 278–285 (2014). <https://doi.org/10.1002/xrs.2550278>
16. B. Deng, G.H. Du, G.Z. Zhou et al., 3D elemental sensitive imaging by full-field XFCT. *Analyst.* **140**, 3521–3525 (2015). <https://doi.org/10.1039/C4AN02401J>
17. L. Li, S.Y. Zhang, R.Z. Li et al., Full-field fan-beam X-ray fluorescence computed tomography with a conventional X-ray tube and photon-counting detectors for fast nanoparticle bioimaging. *Opt. Eng.* **56**, 043106 (2017). <https://doi.org/10.1117/1.OE.56.4.043106>
18. S. Jung, T. Kim, W. Lee et al., Dynamic in vivo X-ray fluorescence imaging of gold in living mice exposed to gold nanoparticles. *IEEE Trans. Med. Imaging.* **39**, 526–533 (2019). <https://doi.org/10.1109/TMI.2019.2932014>
19. S.Y. Zhang, L. Li, J.Y. Chen et al., Quantitative imaging of Gd nanoparticles in mice using benchtop cone-beam X-ray fluorescence computed tomography system. *INT. J. Mol. Sci.* **20**, 2315 (2019). <https://doi.org/10.3390/ijms20092315>
20. C.P. Wu, L. Li, First demonstration of Compton camera used for X-ray fluorescence imaging. *IEEE Trans. Med. Imaging.* **42**, 1314–1324 (2022). <https://doi.org/10.1109/TMI.2022.3226329>
21. S.J. Norton, Compton scattering tomography. *J. Appl. Phys.* **76**, 2007 (1994). <https://doi.org/10.1063/1.357668>
22. M. Bazalova, J.F. Carrier, L. Beaulieu et al., Dual-energy CT-based material extraction for tissue segmentation in Monte Carlo dose calculations. *Phys. Med. Biol.* **53**, 2439 (2008). <https://doi.org/10.1088/0031-9155/53/9/015>
23. W.V. Elmpft, G. Landry, M. Das et al., Dual energy CT in radiotherapy: current applications and future outlook. *Radiother. Oncol.* **119**, 137–144 (2016). <https://doi.org/10.1016/j.radonc.2016.02.026>
24. M. Torikoshi, T. Tsunoo, M. Sasaki et al., Electron density measurement with dual-energy x-ray CT using synchrotron radiation. *Phys. Med. Biol.* **48**, 673 (2003). <https://doi.org/10.1088/0031-9155/48/5/308>
25. N. Hünemohr, B. Krauss, C. Tremmel et al., Experimental verification of ion stopping power prediction from dual energy CT data in tissue surrogates. *Phys. Med. Biol.* **59**, 83 (2013). <https://doi.org/10.1088/0031-9155/59/1/83>
26. N. Hudobivnik, F. Schwarz, T. Johnson et al., Comparison of proton therapy treatment planning for head tumors with a pencil beam algorithm on dual and single energy CT images. *Med. Phys.* **43**, 495 (2016). <https://doi.org/10.1118/1.4939106>
27. M. Yang, P. Wohlfahrt, C.Y. Shen et al., Dual-and multi-energy CT for particle stopping-power estimation: current state, challenges and potential. *Phys. Med. Biol.* **68**, 04TR01 (2023)
28. B.L. Jones, S.H. Cho, The feasibility of polychromatic cone-beam X-ray fluorescence computed tomography (XFCT) imaging of gold nanoparticle-loaded objects: a Monte Carlo study. *Phys. Med. Biol.* **56**, 3719 (2011). <https://doi.org/10.1088/0031-9155/56/12/017>
29. V. Petrillo, A. Bacci, C. Curatolo et al., Polarization of X-gamma radiation produced by a Thomson and Compton inverse scattering. *Phys. Rev. ST. Accel. Beams.* **18**, 110701 (2015). <https://doi.org/10.1103/PhysRevSTAB.18.110701>
30. Z.J. Chi, Polarization transfer from a laser to X rays via Thomson scattering with relativistic electrons: a dipole radiation perspective. *J. Appl. Phys.* **128**, 244904 (2020). <https://doi.org/10.1063/5.0029390>
31. Z.J. Chi, X-ray polarization characteristics in the nonlinear Thomson scattering of a laser with relativistic electrons. *Nucl. Instrum. Meth. A* **1033**, 166681 (2022). <https://doi.org/10.1016/j.nima.2022.166681>
32. Z.J. Chi, Y.C. Du, W.H. Huang et al., Linearly polarized X-ray fluorescence computed tomography based on a Thomson scattering light source: a Monte Carlo study. *J. Syn. Rad.* **27**, 737 (2020). <https://doi.org/10.1107/S1600577520003574>
33. S. Agostinelli, J. Allison, K.A. Amako et al., GEANT4—a simulation toolkit. *Nucl. Instrum. Meth. A* **506**, 250 (2003). [https://doi.org/10.1016/S0168-9002\(03\)01368-8](https://doi.org/10.1016/S0168-9002(03)01368-8)
34. Z.J. Chi, Y.C. Du, W.H. Huang et al., Energy-angle correlation correction algorithm for monochromatic computed tomography based on Thomson scattering X-ray source. *J. Appl. Phys.* **122**, 234903 (2017). <https://doi.org/10.1063/1.4996324>
35. F. Hartemann, W. Brown, D. Gibson et al., High-energy scaling of Compton scattering light sources. *Phys. Rev. ST. Accel. Beams* **8**, 100702 (2005). <https://doi.org/10.1103/PhysRevC.8.044612>
36. Y.C. Du, H. Chen, H.Z. Zhang et al., A very compact inverse Compton scattering gamma-ray source. *High Power Laser Part. Beams* **34**, 104010 (2022). <https://doi.org/10.11884/HPLPB202234.220132>
37. J.A. Bearden, X-ray wavelengths. *Rev. Mod. Phys.* **39**, 78 (1967). <https://doi.org/10.1103/RevModPhys.39.78>
38. K. Taguchi, J.S. Iwanczyk, Vision 20/20: single photon counting x-ray detectors in medical imaging. *Med. Phys.* **40**, 100901 (2013). <https://doi.org/10.1118/1.4820371>
39. L.A. Shepp, Y. Vardi, Maximum likelihood reconstruction for emission tomography. *IEEE Trans. Med. Imaging* **1**, 113 (1982). <https://doi.org/10.1109/TMI.1982.4307558>
40. A. Rose, *Vision: human and electronic* (Plenum Press, New York, 1973), pp.8–12
41. W. Thomlinson, H. Elleaume, L. Porra et al., K-edge subtraction synchrotron X-ray imaging in bio-medical research. *Phys. Med.* **49**, 58–76 (2018). <https://doi.org/10.1016/j.ejmp.2018.04.389>
42. F. Carroll, Tunable, monochromatic X-rays: an enabling technology for molecular/cellular imaging and therapy. *J. Cell Biochem.* **90**, 502–508 (2003). <https://doi.org/10.1002/jcb.10632>
43. K. Yamada, R. Kuroda, R. Kuroda et al., A trial for fine and low-dose imaging of biological specimens using quasi-monochromatic laser-Compton X-rays. *Nucl. Instrum. Meth. A* **608**, S7–S10 (2009). <https://doi.org/10.1016/j.nima.2009.05.157>
44. E. Eggl, K. Mechlem, E. Braig et al., Mono-energy coronary angiography with a compact synchrotron source. *Sci. Rep.* **7**, 42211 (2017). <https://doi.org/10.1038/srep42211>

45. S. Kulpe, M. Dierolf, E. Braig et al., K-edge subtraction imaging for coronary angiography with a compact synchrotron X-ray source. *PLoS. One* **13**, e0208446 (2018). <https://doi.org/10.1371/journal.pone.0208446>
46. Z.J. Chi, Y.C. Du, L.X. Yan et al., K-edge imaging based on a Thomson scattering X-ray source. *Proc. of SPIE* **12169**, 297–304 (2022). <https://doi.org/10.1117/12.2622201>
47. M. Bazalova, Y. Kuang, G. Pratz et al., Investigation of X-ray fluorescence computed tomography (XFCT) and K-edge imaging. *IEEE Trans. Med. Imaging* **31**, 1620–1627 (2012). <https://doi.org/10.1109/TMI.2012.2201165>
48. P. Feng, W.X. Cong, B. Wei et al., Analytic comparison between X-ray fluorescence CT and K-edge CT. *IEEE Trans. Biomed. Eng.* **61**, 975–985 (2013). <https://doi.org/10.1109/TBME.2013.2294677>

Springer Nature or its licensor (e.g. a society or other partner) holds exclusive rights to this article under a publishing agreement with the author(s) or other rightsholder(s); author self-archiving of the accepted manuscript version of this article is solely governed by the terms of such publishing agreement and applicable law.